Supplement of

Mid-Pliocene not analogous to high-CO_2 climate when considering Northern Hemisphere winter variability

Arthur Merlijn Oldeman et al.

Correspondence to: Arthur Merlijn Oldeman (a.m.oldeman@uu.nl)

S1 Spin up of simulations

The equilibration of the CCSM4-Utr simulations presented and analysed in this study is assessed by means of time evolution of the global mean surface temperatures (GMST), shown in Figure S1. The original E^{280} (in gray, before year 0) has had 2,500 years of spin-up, which can be found in the Supplementary material of Baatsen et al. (2022). The E^{280} and E^{560} simulations analysed in this study are denoted as $E^{280,p}$ and $E^{560,p}$, respectively, following the naming convention in Baatsen et al. (2022). It indicates the simulations have been run with a 'paleo' vertical mixing parametrisation that is also employed in the Eoi^{400} and Eoi^{280} simulations (more on that in the Methods section of the main paper).
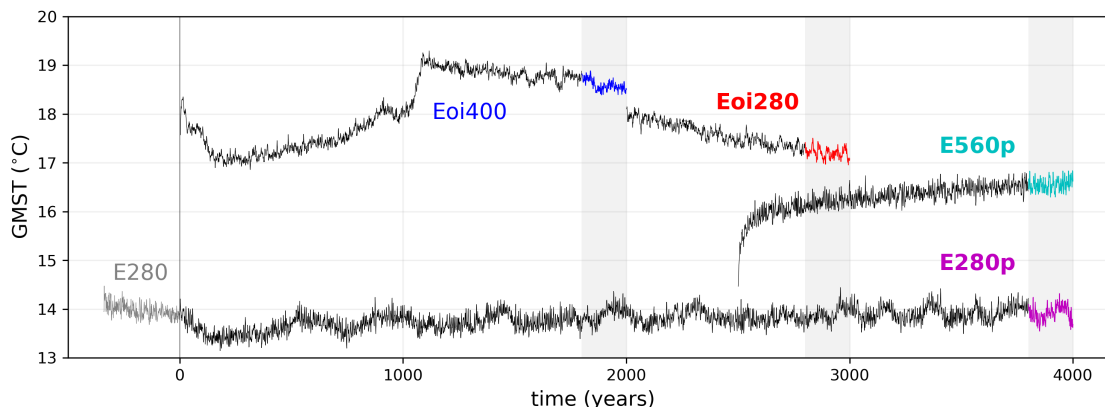
Figure S1: Annual mean global mean surface temperatures (GMST) over simulation years. The colored parts with grey shading are the 200 years that have been used for analysis in this study. In **bold** the simulations presented in the main paper.

S2 Eoi^{400} January SLP results

We will briefly look at winter sea-level pressure (SLP) results for the simulation with mid-Pliocene boundary conditions and mid-Pliocene CO_2 levels, i.e. the Eoi^{400} experiment, that has been featured in many PlioMIP2 studies. Figure S2 show mean SLP (a) and SLP standard deviation (SD, b) for Eoi^{400}, as well as the difference with the E^{280}. The patterns of MSLP increase and decrease are similar to the Eoi^{280} results presented in Figure 2 in the main study. The amplitude of the higher SLP over the North Pacific (up to 16 hPa) is high, considering that the SD of SLP (Figure S2b) in the E^{280} in this region is around 8 hPa. The SLP increase over the North Pacific is also present in the annual mean (as shown by Baatsen et al. (2022)), but with a smaller amplitude (up to 7 hPa). For comparison, the Eoi^{400} simulation performed with CCSM4-UoT also shows a region of higher SLP over the North Pacific in the winter (DJF) mean, that is very similar in amplitude (up to 16 hPa) and spatial extent (Menemenlis et al., 2021). A comparison of the differences between the Eoi^{400} and E^{280} and the other simulations is presented in Figures S11 and S12.

S3 Jet variations in the NH and NP

The analysis of the variations in (latitude of the) jet maximum in the North Pacific as presented in the main paper in Figure 7 is repeated here, but for the global zonal mean
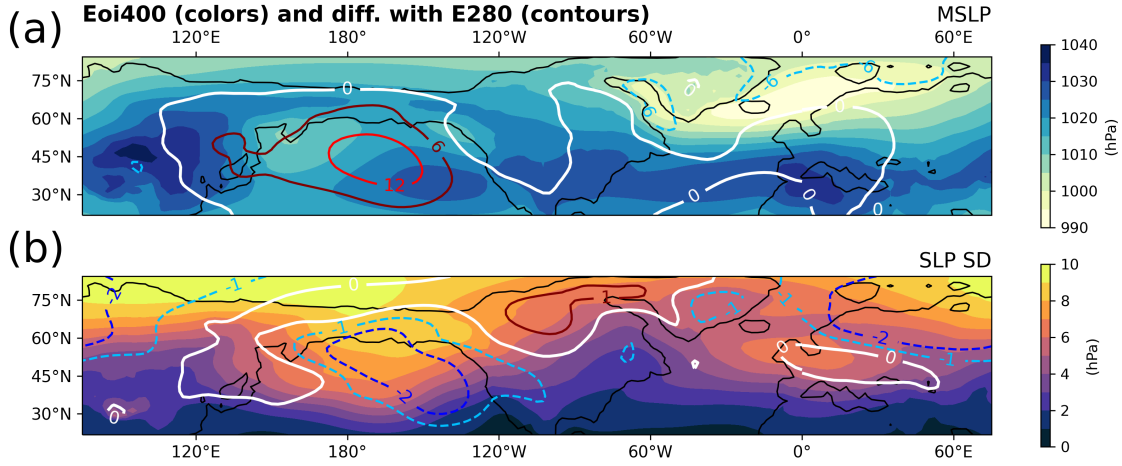
Figure S2: January mean SLP (MSLP, a) and SLP standard deviation (SLP SD, b) for the Eoi^{400} (colors) as well as the difference with E^{280} (contours).

zonal wind and the Arctic Oscillation (AO) mode of variability (Figure S3). The (latitude of the) max jet (Figure S3c and d) is determined per longitude and then averaged to obtain a zonal mean value. Like in the North Pacific, the Eoi^{280} has a smaller range of jet intensities than the E^{280} (Figure S3c). In both climates the AO shows a positive correlation with the jet intensity, and a weak negative correlation with jet latitude. The Eoi^{280} shows a distribution of slightly more poleward latitudes of the strongest jet in Figure S3d when compared to the E^{280}.

Additionally, we repeat the analysis shown in main paper Figure 7 but for the NPO index and jet intensity (Figure S4a) and PNA index and jet latitude (Figure S4b), i.e. the opposite correlations as were presented in main paper Figure 7. Both in the E^{280} and the Eoi^{280}, the NPO index does not correlate with jet intensity (Figure S4a). The scatter shows a cloud of points, and the correlation is not statistically significant (ie p>0.05). A similar picture arises when considering the PNA index and jet latitude (Figure S4b). The correlation is the scatter for the Eoi^{280} is only just statistically significant (at p<0.05, but not significant at p<0.01).

S4   SAT and SLP during the NPO+ and - phases

Figure S5 is an extension of Figure 9 in the main study, showing the surface impacts of the NPO- and NPO+ phases in the E^{280} and Eoi^{280} simulations by means of SAT anomalies (colors) and SLP anomalies (contours). The NPO+ phase is defined as the average of the top 5% (or ten Januaries) NPO PC values, and the NPO- phase as the average of the bottom 5% NPO PC values.

S5   Linking WEP convection to NP variability via Rossby wave activity

This section presents some additional analyses to the dynamical hypothesis proposed in the main paper in section 3.3.3 "Tropical Pacific convection as an explanation".
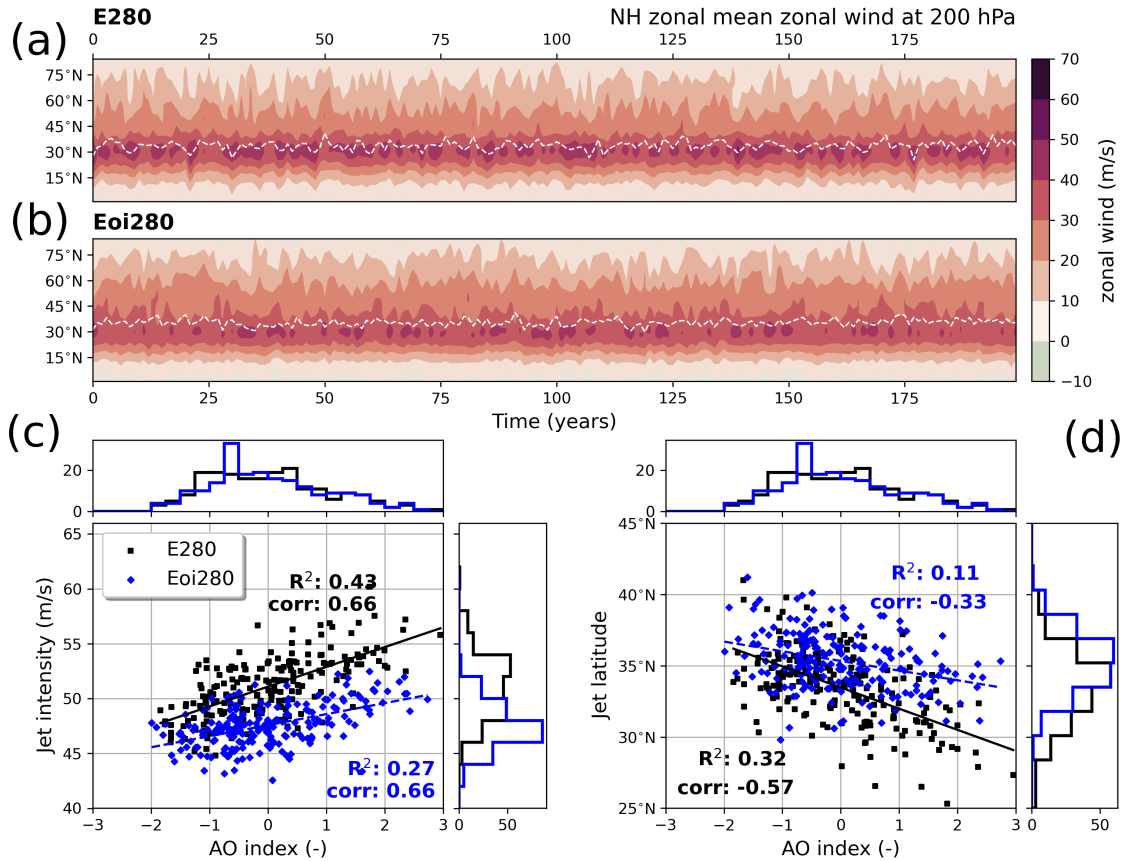
Figure S3: (a,b) Hovmöller diagrams showing NH zonal mean zonal wind at 200 hPa for every January for the E^{280} (a) and Eoi^{280} (b). The white dashed line follows the maximum of zonal wind. (c) Scatter plot including histograms of counts for the AO index versus the jet intensity (defined as mean of the max zonal wind per longitude). R^2 of linear fit and correlation coefficient are shown. For E^{280} (black squares) and Eoi^{280} (red diamonds). (d) Same, but for AO index versus jet latitude (defined at mean latitude of max zonal wind per longitude).

S5.1   ENSO and WEP precipitation

Figure S6 shows the regression between the January Nino3.4 index and the precipitation anomalies in the pre-industrial reference E^{280} simulation (values only shown when p<0.05). It shows that the strongest positive regression between ENSO variability and precipitation anomalies concentrates in the west-equatorial Pacific (WEP) region, highlighted in cyan. The regression is similar for the Eoi^{280}. This result motivated us to use the mean precipitation in the WEP region as a measure of the tropical convection related to ENSO variability.

S5.2   Changes to upper-tropospheric Rossby wave activity

We want to investigate the precise link between the WEP precipitation and the NP jet stream and SLP variations (as shown in main paper Figure 9b,c) using the Rossby Wave Source (RWS, Nie et al., 2019). The RWS is a measure of upper-tropospheric vorticity sources and sinks. Anomalous convection in the tropics can lead to anomalous vorticity in the subtropical upper-troposphere, through the Hadley circulation. This anomalous vorticity can be a source (or sink) of atmospheric Rossby waves.

3
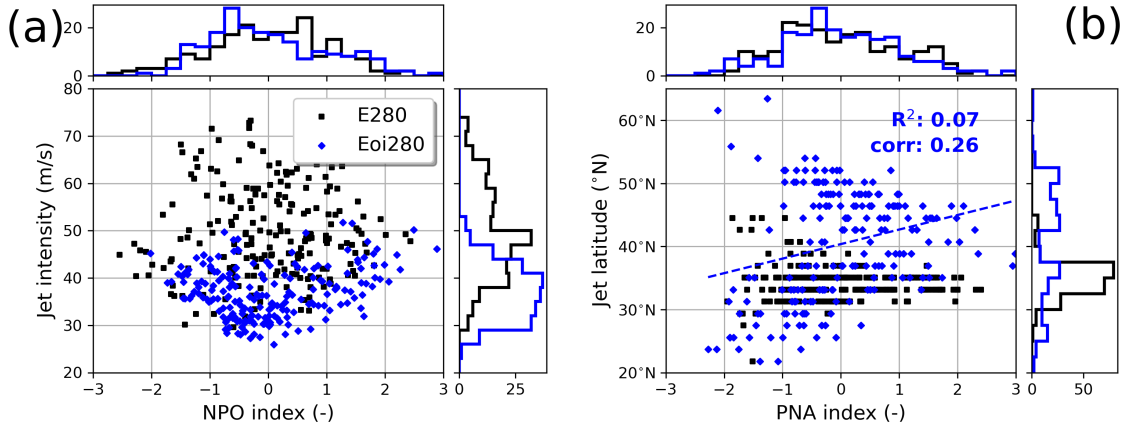
Figure S4: Same as for Figure S3c and d, but for NPO index and jet intensity (a) and PNA index and jet latitude (b). All scatters except for the Eoi^{280} PNA vs jet latitude do not have a statistically significant correlation (defined as p<0.05)

Following Nie et al. (2019), we compute the RWS using the zonal and meridional wind fields at 200hPa:

$$RWS_{tot} = -\nabla \cdot (\mathbf{v_x}\zeta_a) = -\zeta_a \nabla \cdot \mathbf{v_x} - \mathbf{v_x} \cdot \nabla\zeta_a \tag{1}$$

where $\mathbf{v_x}$ is the horizontal wind vector and ζ_a the vertical component of absolute vorticity. The first term on right hand side ($-\zeta_a \nabla \cdot \mathbf{v_x}$) represents vortex stretching, or the impact of the upper-tropospheric divergence pattern on the vorticity change. We will call this part RWS_{VS}. The second term on right hand side ($-\mathbf{v_x} \cdot \nabla\zeta_a$) represents advection of absolute vorticity by the divergent wind flow. We compute the RWS, we use the python package windspharm (Dawson, 2016).

First, we show in Figure S7 that indeed, the precipitation in the WEP has a significant correlation and regression signal with the RWS_{VS} in the E^{280}. The regression is shown for the RWS_{VS} term, as the signal was found to be the strongest for the vortex stretching component. This is not entirely surprising, as it is mainly the vortex stretching RWS term that relates to the tropical convection, through subtropical upper-troposphere convergence from the descending branch of the Hadley circulation. The strongest positive regression is found over the region of the East Asian jet exit. There is a small correlation in the northwestern Pacific, which is a Rossby wave sink related to wave breaking.

Secondly, we will show how the RWS_{tot} and RWS_{VS} change in the Eoi^{280}. These results are shown in Figure S8. Figure S8a shows the time-average RWS in the E^{280} at 200hPa. It shows a large Rossby wave source over East Asia, and a strip of Rossby wave sink over the North Pacific. Figure S8b shows the difference of the total RWS with the Eoi^{280}. It can be seen that there is a reduction of the main RW source over East Asia, and decrease in RWS over the western NP, indicating a reduction of the RW sink. Figure S8c shows the RWS_{VS} in the E^{280}. It can be seen that most of the strength of the RW source and RW sinks is dominated by the vortex stretching term. Figure S8d shows the difference of the RWS_{VS}. Again, most of the total RWS difference is related to the vortex stretching. However, the reduction of the East Asia RW source is stronger. It is expected that a reduction of the RW source over East Asia leads to a reduction of the RW sink over the North Pacific; reduced Rossby wave activity means less sources and thus less sinks.

4

S5.3 East Asia Rossby wave source and jet stream variability

Figure S9 shows the regression of the vortex stretching contribution to the RWS in East Asia (averaged in the cyan rectangle drawn in Figure S8c,d) with the SLP (colors) and zonal wind (contours), for the E^{280} (a) and Eoi^{280} (b). It is essentially a repetition of main paper Figure 9b and c, but now the regression is with the RWS_{VS} in East Asia instead of the WEP precipitation. The regression patterns with SLP and zonal wind is very similar to Figure S8c,d. Whereas the Rossby wave source over East Asia is the direct driver to jet stream variability, and thus SLP variability, the WEP precipitation is a more indirect driver, as it influences the Rossby wave activity (through Figures S7 and S8)

S6 Energy budget analysis

We use a simple energy balance model to evaluate the dominant components of warming in the E^{560} and Eoi^{280} simulations, with respect to the E^{280} reference. We assess the temperature contributions from the different components in the radiative budget, repeating the analysis in Baatsen et al. (2022), which follows the methods of Hill et al. (2014). The energy balance model is based on a radiative budget framework by Heinemann et al. (2009). The top-of-model (TOM) radiative budget is as follows:

$$S(1 - \alpha_p) + H = \epsilon \sigma \tau^4 \tag{2}$$

where S is the incoming solar radiation, α_p the planetary albedo, H the meridional heat transport, ϵ the effective emissivity, σ the Stefan-Boltzmann constant and τ the surface temperature. This equation can be rearranged to obtain the surface temperature. The contribution of one term (e.g. planetary albedo changes) to the warming between two simulations can then be estimated. The sum of the contributions of the planetary albedo (representing SW fluxes at TOM), meridional heat transport and effective emissivity (representing LW fluxes at TOM) generally explains almost all of the temperature differences. We consider the 2D fields of the monthly climatologies. We consider the (contributions to the) warming between the E^{560} - E^{280}, and Eoi^{280} - E^{280}. We focus on the results in January (as in the main manuscript). We present the effective emissivity split into the contribution of longwave cloud radiative forcing (*Emiss.: LW cloud*), and the sum of clearsky contributions, e.g. due to greenhouse gases and lapse rate feedbacks (*Emiss.: clearsky*).

The main contribution to the warming in the E^{560} simulation is the clearsky effective emissivity (Figure S10g). The majority of this emissivity contribution is caused by the increased radiative forcing from the doubled atmospheric CO_2. Around Greenland and the Siberian Arctic, there is an emissivity contribution from the LW cloud forcing (Figure S10e). Where sea ice retreats, there is more local evaporation, which leads to more precipitation and cloud cover, that effectively keep longwave radiation at the surface, acting as a warming contribution. The planetary albedo contribution is small (Figure S10c). There is a small, positive, contribution from the meridional heat transport, especially over the Arctic (Figure S10g).

In the Eoi^{280}, most of the warming is explained by the contributions related to planetary albedo (Figure S10d) as well as clearsky effective emissivity (Figure S10h). CO_2 is not increased, but there is still a greenhouse gas contribution from water vapour changes, as well as changes due to lapse rate feedbacks. Even though the Greenland ice sheet is reduced,

the planetary albedo contribution in the higher latitudes is small, since in January the incoming solar radiation is at a minimum in the Northern Hemisphere. In the annual mean (Baatsen et al. (2022), Figure 11), the planetary albedo contribution in the higher latitudes is more substantial. Most planetary albedo contributions over land are related to changes in vegetation and lakes. In the higher latitudes there is again a substantial contribution from longwave cloud radiative forcing (Figure S10f). In the (sub)tropics, there are large feedbacks related to the shifts in the ITCZ and Walker circulation. Over the West equatorial Pacific, convection and precipitation decreases, leading to lower cloud cover, reducing the planetary albedo and thus leading to a warming component from more incoming solar radiation. However, the reduced cloud cover also decreases effective emissivity because more longwave radiation is lost. These contributions largely cancel out. Again, there is a small, positive, contribution from the meridional heat transport over the Arctic (Figure S10h).

In both cases, the sign of the contribution of the meridional heat transport to the total warming seems unintuitive. A weaker meridional temperature gradient should result in a weaker meridional heat transport from the equator to the poles, effectively cooling the higher latitudes. Indeed, this is the case for the annual mean zonal mean (Baatsen et al. (2022), Figure 11). However, in January, the warming contribution is positive, especially over the higher latitudes, for both the E^{560} and Eoi^{280}. This suggests that changes in atmospheric transport contribute to a warming in the higher latitudes, in both simulations, which is not intuitive considering the changes in surface temperature gradient alone. It should be noted that the input in this energy balance model are shortwave and longwave fluxes, and the meridional heat transport term is used to close the energy budget. In other words, the meridional heat transport is not calculated. It is possible that the actual energy budget is not entirely closed since we are considering the situation in January on one hemisphere. A brief look at the modelled heat fluxes (not shown) does reveal that changes in sensible and latent heat fluxes can explain some of the MHT response, so it is not just a artefact of closing the energy budget.

S7 Additivity of simulation responses

This section explores the additivity of the mean SLP and SLP SD responses to different boundary conditions and CO_2 levels. We explore the following set of simulation differences:

- E^{560} - E^{280}: response to CO_2 doubling in a pre-industrial climate

- Eoi^{560} - Eoi^{280}: response to CO_2 doubling in a mid-Pliocene climate

- Eoi^{280} - E^{280}: response to mid-Pliocene boundary conditions at low CO_2

- Eoi^{560} - E^{560}: response to mid-Pliocene boundary conditions at high CO_2

- Eoi^{400} - E^{280}: response to mid-Pliocene climate (PlioMIP2)

Figure S11 shows the difference in mean SLP and Figure S12 shows the difference in SLP SD. The results are treated briefly in the main paper Discussion.

References

Baatsen, M. L. J., von der Heydt, A. S., Kliphuis, M. A., Oldeman, A. M., and Weiffenbach, J. E. (2022). Warm mid-Pliocene conditions without high climate sensitivity: the CCSM4-Utrecht (CESM 1.0.5) contribution to the PlioMIP2. *Climate of the Past*, 18(4):657–679.

Dawson, A. (2016). Windspharm: A high-level library for global wind field computations using spherical harmonics. *Journal of Open Research Software*, 4(1).

Heinemann, M., Jungclaus, J. H., and Marotzke, J. (2009). Warm Paleocene/Eocene climate as simulated in ECHAM5/MPI-OM. *Clim. Past*.

Hill, D. J., Haywood, A. M., Lunt, D. J., Hunter, S. J., Bragg, F. J., Contoux, C., Stepanek, C., Sohl, L., Rosenbloom, N. A., Chan, W.-L., Kamae, Y., Zhang, Z., Abe-Ouchi, A., Chandler, M. A., Jost, A., Lohmann, G., Otto-Bliesner, B. L., Ramstein, G., and Ueda, H. (2014). Evaluating the dominant components of warming in Pliocene climate simulations. *Climate of the Past*, 10(1):79–90.

Menemenlis, S., Lora, J. M., Lofverstrom, M., and Chandan, D. (2021). Influence of stationary waves on mid-Pliocene atmospheric rivers and hydroclimate. *Global and Planetary Change*, 204(July).

Nie, Y., Zhang, Y., Yang, X., and Ren, H. (2019). Winter and Summer Rossby Wave Sources in the CMIP5 Models. *Earth and Space Science*, 6(10):1831–1846.
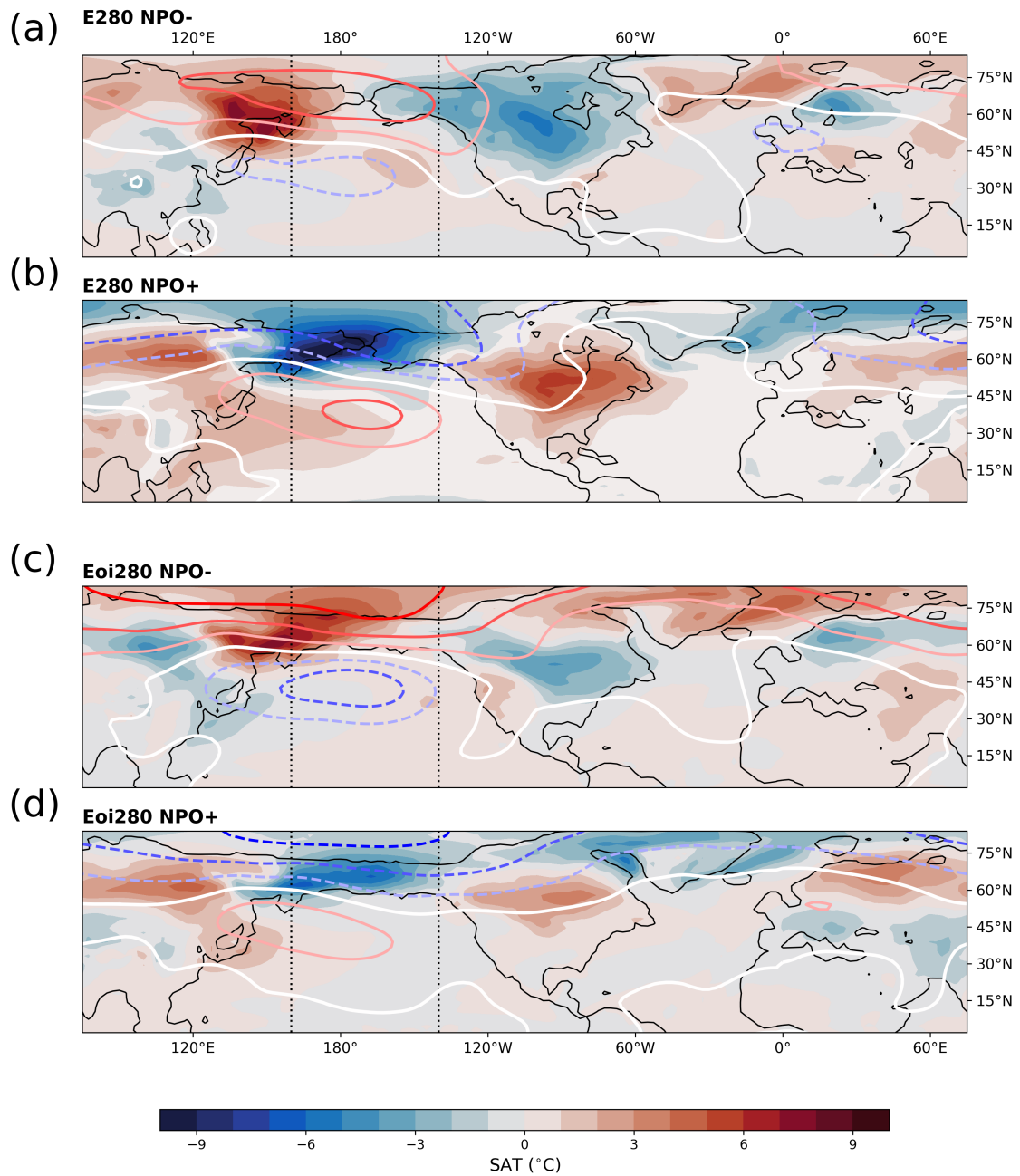
Figure S5: Surface air temperature (SAT, colors) and sea-level pressure (SLP, contours) anomalies (to the January mean). For the E^{280} (a, b) and Eoi^{280} (c, d), representing the NPO- phases (a, c) and NPO+ phases (b, d). SLP anomalies in steps of 5 hPa, white is zero, blue means negative, red means positive.
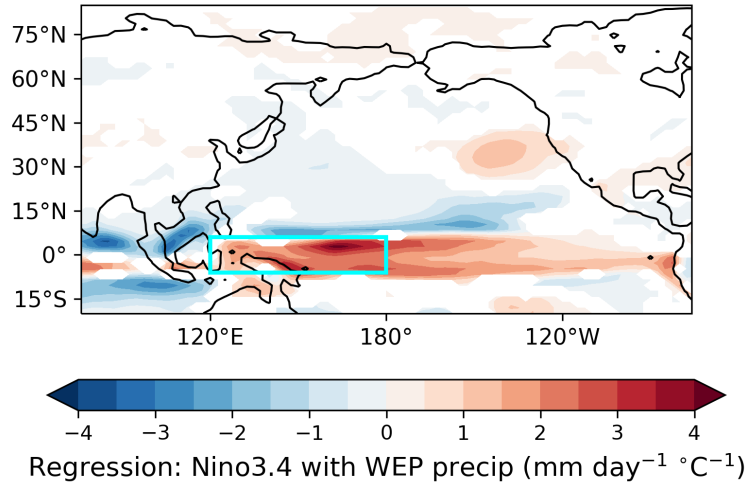
Figure S6: E^{280}: Regression (linear slope) of ENSO variability (defined through Nino3.4 index) with precipitation anomalies. Box drawn is the west equatorial Pacific (WEP). Regression only shown when correlation is significant ($p<0.05$).
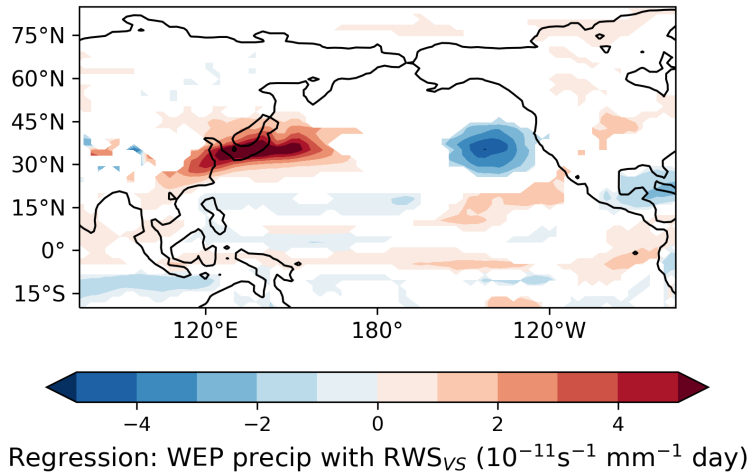
Figure S7: E^{280}: Regression (linear slope) of precipitation in the west equatorial Pacific (WEP) with the vortex stretching component of the Rossby wave source RWS_{VS}. Regression only shown when correlation is significant ($p<0.05$).
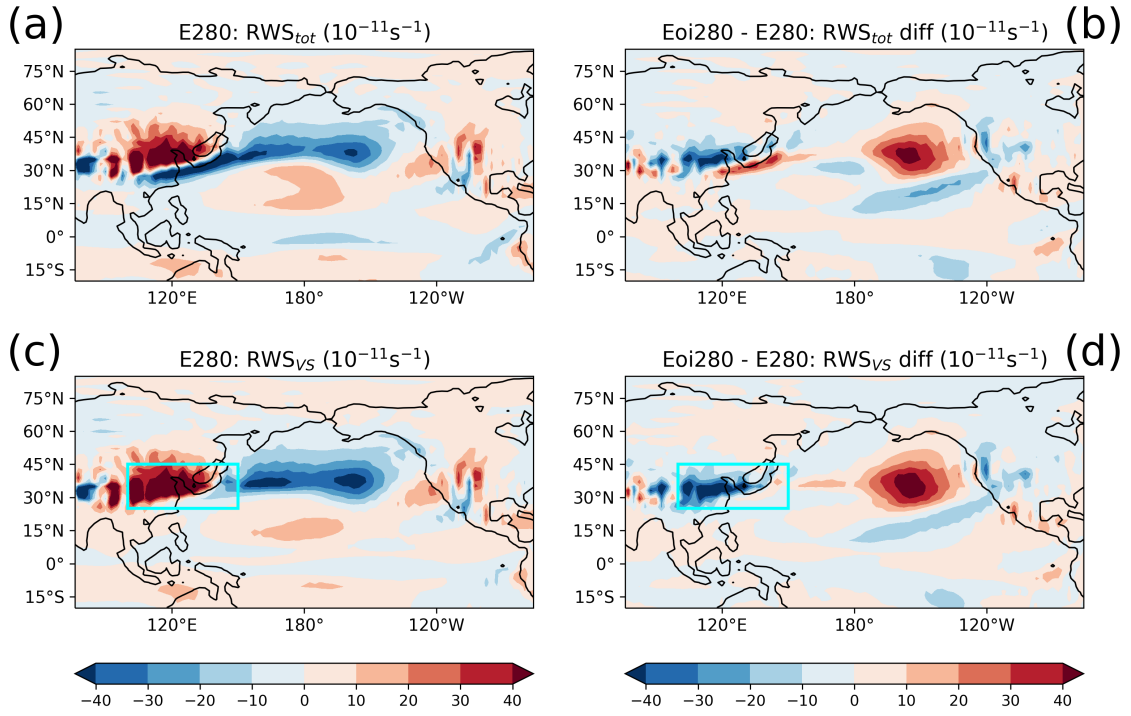
Figure S8: January mean total RWS in E^{280} (a), total RWS difference between Eoi^{280} and Eoi^{280} (b), vortex stretching contribution to RWS (RWS$_{VS}$) in E^{280} (c) and RWS$_{VS}$ difference between Eoi^{280} and Eoi^{280} (d). Box drawn in (c) and (d) is the East Asia sector.
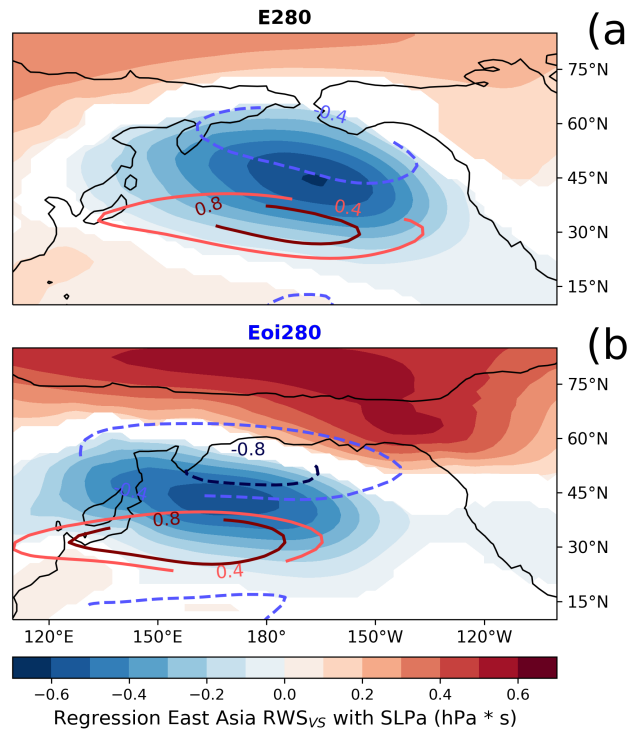
Figure S9: Regression (linear slope) between vortex stretching term of the RWS averaged over East Asia (RWS$_{VS}$) and SLP anomalies (colors), and WEP precipitation and zonal wind at 200 hPa (contours), for E^{280} (a) and Eoi^{280} (b). Regression only shown when correlation is significant (p>0.05).
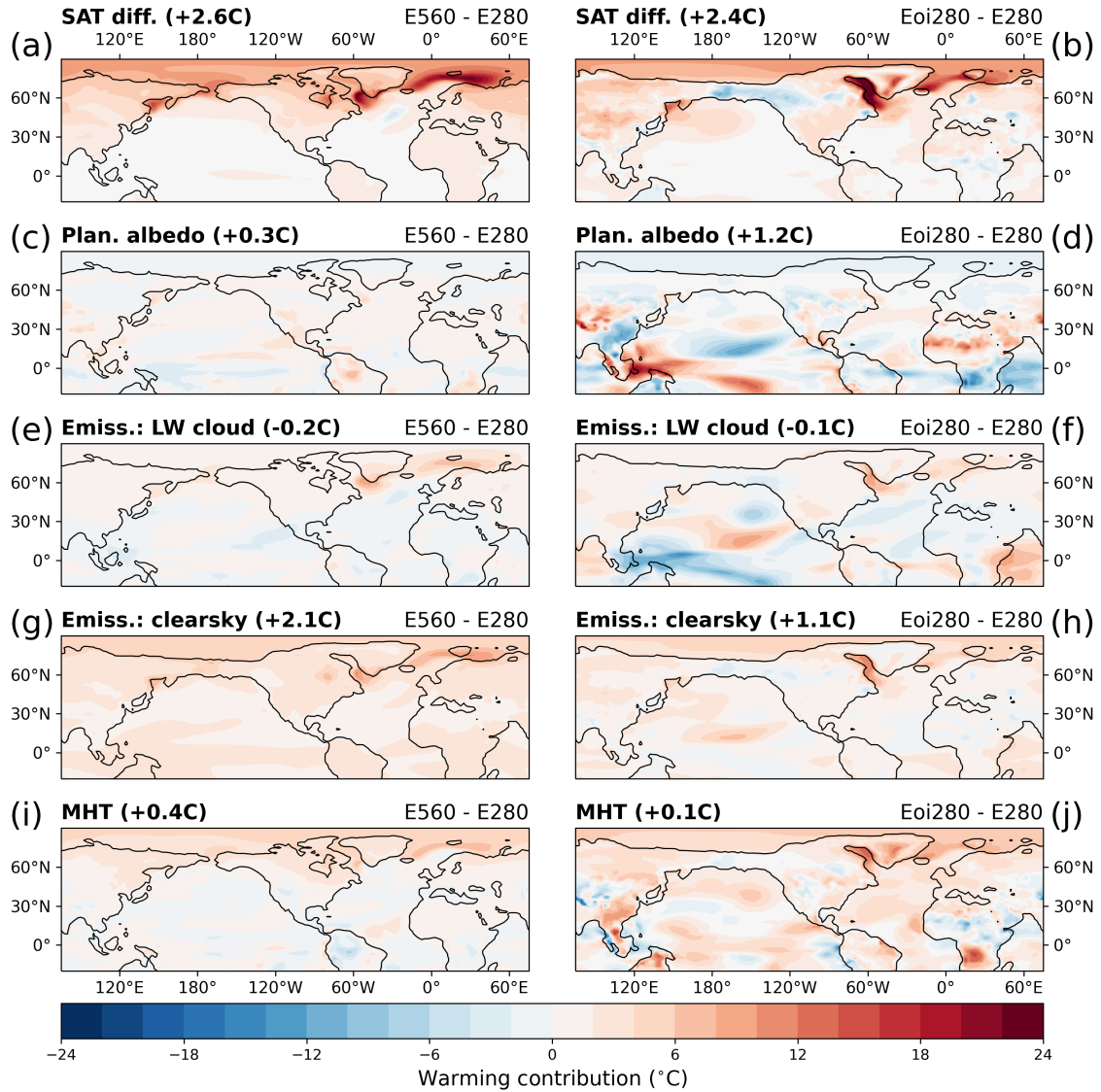
Figure S10: Energy budget analysis. Surface warming differences between (a) E^{560} - E^{280} and (b) Eoi^{280} - E^{280} (as in main paper Figure 3). (c-j) contributions to the warming according to the top-of-model energy balance model. (c, e, g, i) E^{560} - E^{280} and (d, f, h, j) Eoi^{280} - E^{280}. (c,d) planetary albedo, (e,f) effective emissivity due to clouds, (g,h) effective emissivity at clearsky conditions (e.g. due to greenhouse gases and lapse rate feedbacks), and (i,j) meridional heat transport (MHT). In (brackets) the mean temperature contribution, averaged over 20S - 90N.
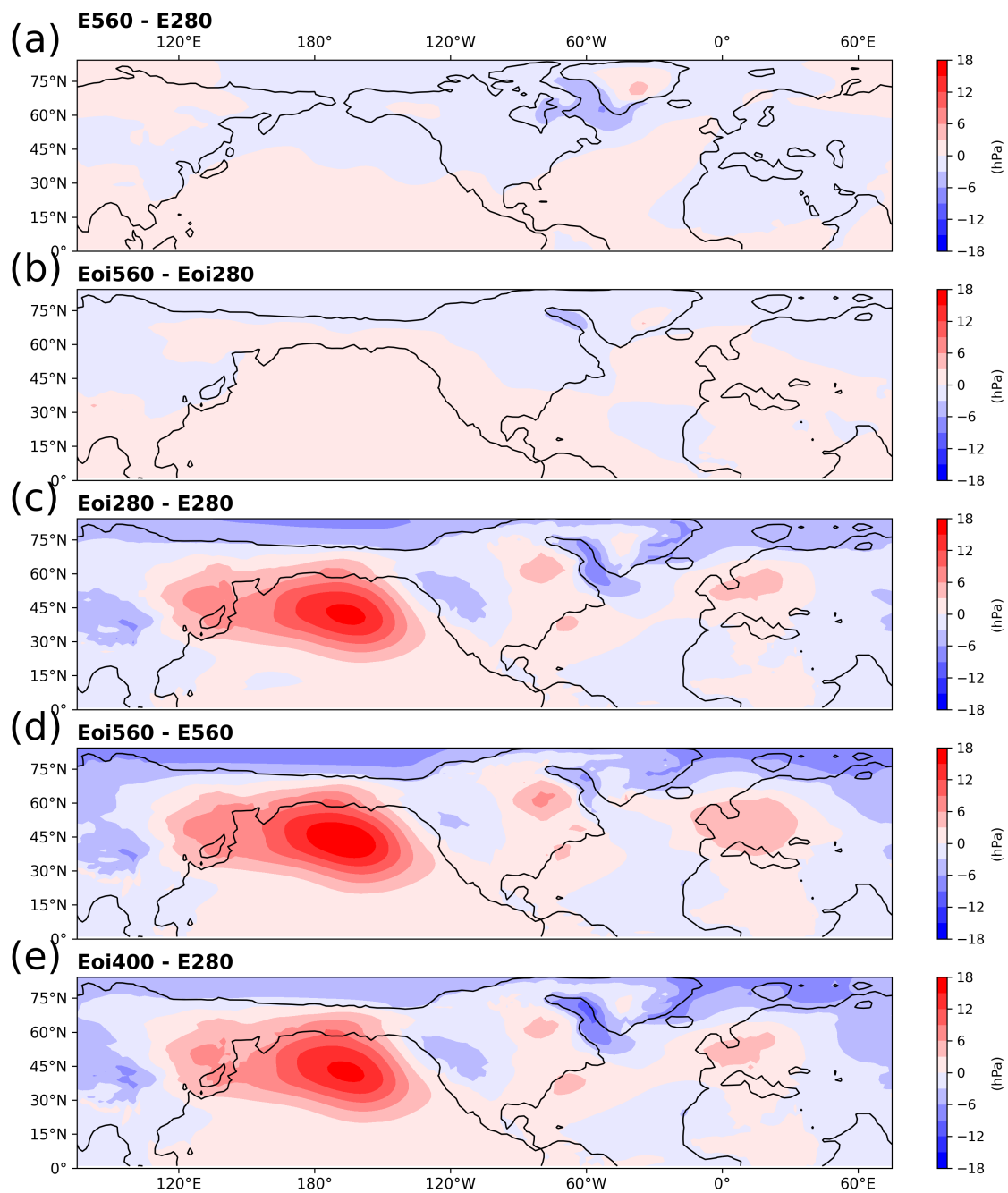
Figure S11: January mean SLP differences for a set of simulations.
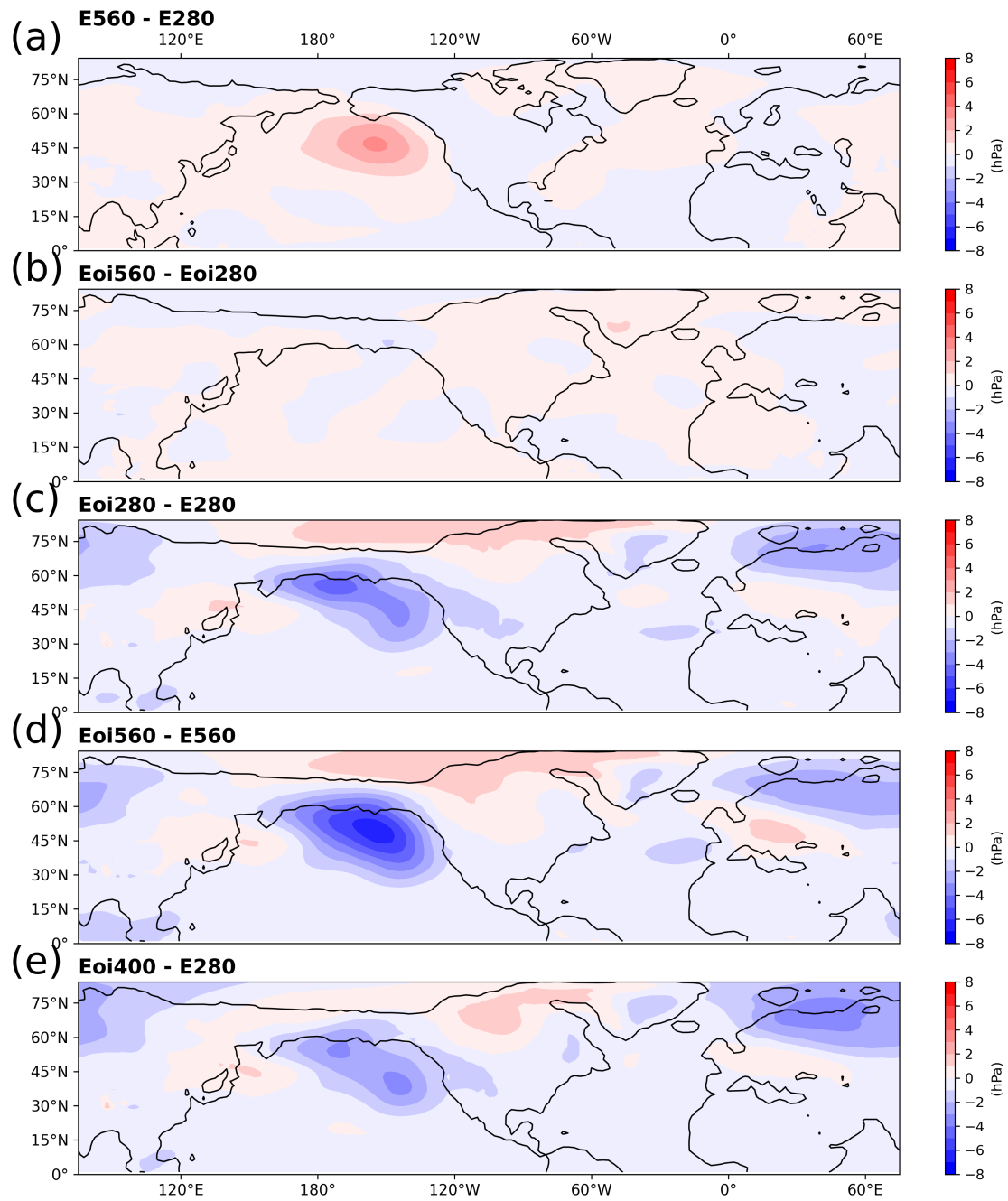
Figure S12: January SLP SD differences for a set of simulations.